Electrostatic manipulation of phase behavior in immiscible charged polymer blends

Journal:	*Macromolecules*
Manuscript ID	ma-2021-000952
Manuscript Type:	Article
Date Submitted by the Author:	13-Jan-2021
Complete List of Authors:	Grzetic, Douglas; University of California Santa Barbara, Delaney, Kris; University of California Santa Barbara, Materials Research Laboratory Fredrickson, Glenn; University of California Santa Barbara, Materials Research Laboratory;

Electrostatic manipulation of phase behavior in immiscible charged polymer blends

Douglas J. Grzetic,*,† Kris T. Delaney,*,† and Glenn H. Fredrickson*,†,‡

†*Materials Research Laboratory, University of California, Santa Barbara, California 93106, USA*

‡*Departments of Chemical Engineering and Materials, University of California, Santa Barbara, California 93106, USA*

E-mail: dgrzetic@mrl.ucsb.edu; kdelaney@mrl.ucsb.edu; ghf@ucsb.edu

Abstract

Microphase separation in a binary blend of oppositely charged polymers can in principle be stabilized electrostatically, without the need for connected block polymer architectures. This provides a route to control microstructure via parameters such as polymer charge density, salt concentration and dielectric constant. Here, we use equilibrium self-consistent field theory to study the phase behavior of such a binary blend, with or without counterions and added salt, and show that it exhibits the canonical ordered phases of a diblock copolymer melt. We demonstrate how differences in the charge density and the dielectric constant of the two polymers affect phase behavior in this system. In particular, we find that the phase windows for sphere phases are dramatically affected, and that the Frank-Kasper phases σ and $A15$ can be stabilized when the minority component has a higher dielectric constant than the surrounding matrix. Since the domain length scale in this system is determined electrostatically and is not subject to chain-stretching limitations imposed by block architectures, our results suggest a possible route to large-unit-cell complex-sphere phases. These predictions will be most easily tested in oppositely charged polymeric ionic liquids, where the bulky and de-localized charges should aid equilibration in a solvent-free environment.

Introduction

The widespread interest in inhomogeneous multi-component polymeric systems has been largely motivated by the ability to combine components with different desirable properties into one material. Thermoplastic elastomers are perhaps the most well-known example of this: they leverage block architectures, and combine a glassy block with a rubbery block to achieve a material with simultaneous toughness and elasticity.[1] In such materials, the block connectivity prevents the often immiscible components from macrophase separating, leading to ordered micro-structures whose symmetry and length-scale are determined by architectural properties such as the number and sequence of blocks and their molecular weights. In recent years, ion-containing polymeric components have drawn much attention as a way to further modify the structural properties of the material and introduce new functionalities; this has led to a growing interest in polyelectrolyte complexes,[2,3] salt-doped polymers,[4–7] ionomers[8,9] and polymeric ionic liquids[10–13] (PILs) as a route to grant the material high ionic conductivity, stimuli-responsiveness, magnetic or optical properties, etc.

The incorporation of ions into polymeric systems is also known to strongly affect the phase behavior, through the electrostatic interactions of the ionic components with each other as well as with the other (polar and non-polar) components. This is challenging from a theory and modeling standpoint, as it introduces the need to consider a range of related electrostatic phenomena such as local dielectric response, ion solvation, van der Waals interactions, electrostatic screening, and ion correlation effects. Most theories to date have fallen short of accounting for all of these in a self-consistent manner. Despite the theoretical challenges, such systems present an opportunity for manipulation of phase behavior by exploring 'electrostatic' axes (i.e. changing charge densities, dielectric constants, salt content, etc.) without the need to change molecular architecture. For example, in a salt-doped block copolymer where the components have different dielectric constants, the thermodynamic preference of ions to be solvated by the higher-dielectric component leads to a driving force for phase separation that can be exploited to access different morphologies by changing salt-loading. Such a strategy can stabilize phases that would normally be difficult or impossible to access by varying the temperature or polymeric composition alone.[4] A notable recent illustration is the stabilization, by salt-doping, of a giant unit-cell $C15$ Laves phase in an A/B/AB ternary blend.[14]

Significant theoretical efforts have been undertaken to predict how the incorporation of ions affects the phase behavior of polymers, with varying degrees of success. For salt-doped polymers that are otherwise charge-neutral, most of these efforts have used variants of polymer self-consistent field theory (SCFT) in which the critical ion-solvation effects are inserted by supplementing the usual SCFT Hamiltonian with a solvation energy term based on the Born solvation approximation.[15–19] Indeed, a mean-field treatment of electrostatics (in effect equivalent to Poisson-Boltzmann theory) is by itself insufficient to capture the effects of ion solvation on phase behavior, which are understood to require field fluctuations.[20,21] Similarly, there are a wide range of related systems containing charged polymeric components, in which the relevant electrostatic effects arise from charge correlations, and lead to phase behavior that is dramatically different from any charge-neutral polymeric counterpart. Examples include polyelectrolyte and copolyelectrolyte solutions, in which charge correlations can drive the formation of disordered and structured "complex coacervates". Theoretical treatments of these cases necessitate either including fluctuation effects explicitly (by conducting field-theoretic[22,23] or particle-based[24,25] simulations) or implicitly (by conducting hybrid simulations that couple the computationally-convenient SCFT with another theory, such as liquid state theory, that can embed the correlation/fluctuation effects).[26–29]

It has been noted by a number of researchers[30–35] that it is possible in principle to exploit electrostatic interactions in charged polymer blends or solutions, in order to *electrostatically* stabilize microphases. Essentially, the immiscibility of the components drives phase separation, but the accumulation of charge in the resulting domains prohibits their unbounded growth (due to a diverging electrostatic energy cost for the charge separation) and thus prevents macrophase separation, leading to ordered microphases instead. This intriguing idea, which has received relatively little attention, provides an alternative to the paradigm of using block architectures to achieve micro-structures, and the symmetry and length-scale of the resulting morphologies are determined electrostatically and can be decoupled from the architectural properties of the polymers. It is important to note that if the counterions present in the system localize and charge-neutralize the respective domains, the phase separation is not accompanied by net charge accumulation and macrophase separation is once again permitted. Such a system will possess a Lifshitz point, the location of which will depend on parameters such as counterion/salt concentration.

Borue and Erukhimovich[30] were the first to point out this notion of electrostatically-stabilized microphase separation: they applied the random phase approximation (RPA) to a polyelectrolyte solution and showed that, under certain conditions of solvent quality and salt concentration, microphases with domains rich and poor in polyelectrolyte were stabilized. Later, Dobrynin and Erukhimovich[31] extended this idea to a melt of weakly charged and uncharged immiscible polymers, and computed mean-field (RPA) and fluctuation-corrected phase diagrams using the Brazovskii-Fredrickson-Helfand[36,37] (BFH) approach. More recently, Rumyantsev and co-workers have extended these ideas to solutions[32,33] and melts[34,35] of immiscible oppositely-charged polyelectrolytes, considered ion-binding and dielectric asymmetry effects,[32] and explored the analogy between this class of charged polymer system and the canonical diblock copolymer, in particular regarding their phase behavior, domain spacing and fluctuation effects.[34,35] However, much of this work has relied on analytical approximations that invoke weak or strong segregation assumptions, and are limited to considering the simplest ordered phases such as body-centered cubic spheres (BCC), hexagonally-packed cylinders (C), and lamellar (L) phases. The only calculations that go beyond these approximations (such as the dissipative particle dynamics simulations of Ref. 34) mainly served to verify the analytical predictions, and a comprehensive phase diagram for this type of system has not been computed to date.

In this work, we relax many of the previously made approximations and construct a field-theoretic model for a blend of oppositely-charged polymers, with associated counterions, that is suitable for full self-consistent field theory (SCFT) calculations, or even fully-fluctuating field-theoretic simulations (FTS) if fluctuation effects are of interest. The model accounts for the effects of dielectric contrast, using a polarizable field theory framework,[21,38–42] as well as the concomitant ion solvation effects. Since the phenomenon that we are interested in (electrostatically-stabilized microphase separation) is caused by the formation of domains that have *non-zero* net charge, a mean-field (SCFT) treatment of the electrostatics is in fact an appropriate starting point. This is in contrast to many other phenomena of interest involving charged polymers, such as the aforementioned polyelectrolyte coacervation, for which the phases of interest are charge-neutral and thus incorrectly attributed by mean-field theory to have zero electrostatic energy. Here, we apply SCFT to the model, which allows us to conveniently map the phase behavior, and we present the first comprehensive phase diagrams for this system. In addition to the simple phases BCC, C and L, we consider the double gyroid phase (G), face-centered cubic (FCC) spheres, and the Frank-Kasper phases σ and $A15$. In addition to computing the phase diagram for the electrostatically-symmetric case (equal and opposite charge densities, with zero dielectric contrast), we also consider how asymmetries in the charge densities and dielectric constants affect the phase behavior in this system. The ion solvation effects, which are important when there is dielectric contrast between domains, are treated here by Taylor expanding the Born solvation energy in powers of the dielectric contrast, and showing that they can be embedded in the form of χ parameters between the counterions and the polymers. Our SCFT results indicate that electrostatic asymmetries have the biggest effect on the spherical phases, and in the case of dielectric asymmetry, can be used to stabilize Frank-Kasper phases, providing a new potential route to such exotic phases in multi-component polymeric systems.

Theory and Methods

Molecular model

We consider an incompressible melt containing n_A polycations of species A, and n_B polyanions of species B, which for simplicity we model as continuous Gaussian chains having the same degree of polymerization N and statistical segment length b. The polymer charge densities are $\sigma_A \geq 0$ and $\sigma_B \leq 0$, and the system also contains n_+ and n_- small-molecule cations and anions, respectively, which include the (monovalent) counterions and any excess salt. Note here that the charge on each polymer ($Q_{A/B} = \sigma_{A/B} N$) is uniformly smeared along the backbone. We will primarily be concerned here with the salt-free 'stoichiometric' case in which each chain of either species is accompanied by a set of charge-neutralizing monovalent counterions, such that $n_- = n_A |\sigma_A| N$ and $n_+ = n_B |\sigma_B| N$, but our model can also accommodate excess salt and the removal of counterions, subject to the overall electroneutrality constraint $N(n_A\sigma_A + n_B\sigma_B) + n_+ - n_- = 0$. The average total number density of polymer segments and small-molecule ions in the system is thus $\rho_0 = (n_A N + n_B N + n_+ + n_-) V^{-1}$, where V is the system volume. The canonical partition function can be written as

$$\mathcal{Z}_c = \frac{1}{n_A! n_B! n_+! n_-! \lambda_T^{3(n_A N + n_B N + n_+ + n_-)}} \int \prod_{i,j=1}^{n_A,n_B} \mathcal{D}\mathbf{r}_i \mathcal{D}\mathbf{r}_j \prod_{k,l=1}^{n_+,n_-} d\mathbf{r}_k d\mathbf{r}_l \exp\left(-\beta U_0 - \beta U_1 - \beta U_c\right) \times \delta\left[\check{\rho}_A(\mathbf{r}) + \check{\rho}_B(\mathbf{r}) + \check{\rho}_+(\mathbf{r}) + \check{\rho}_-(\mathbf{r}) - \rho_0\right], \quad (1)$$

where λ_T is the thermal wavelength, and the $\check{\rho}$ are smeared microscopic density operators given by

$$\check{\rho}_{A/B}(\mathbf{r}) = \sum_{i=1}^{n_{A/B}} \int_0^N ds\, \Gamma(\mathbf{r} - \mathbf{r}_i(s)) \quad (2)$$

for the polymer densities, and

$$\check{\rho}_{+/-}(\mathbf{r}) = \sum_{i=1}^{n_{+/-}} \Gamma(\mathbf{r} - \mathbf{r}_i) \tag{3}$$

for the small-molecule cation and anion densities. Note that these smeared density operators have the usual delta functions replaced by normalized Gaussians $\Gamma(\mathbf{r}) = (2\pi a^2)^{-3/2} \exp(-r^2/2a^2)$, where we fix the smearing range to be $a/R_g = 0.2$, $R_g = b\sqrt{N/6}$ being the ideal-chain radius of gyration for the polymers. The smearing of densities in this model is a strategy for rendering the resulting field theory ultraviolet-convergent.[20,43] Although in this work we study the model using SCFT, which does not require a UV-convergent model, we nonetheless use a smeared model in order to facilitate future studies of the same model using fully-fluctuating FTS (which does require UV-convergence).[44]

The bonded interaction energy U_0 in eq 1, for the continuous Gaussian chain model, is given by

$$\beta U_0 = \sum_{i=1}^{n_A+n_B} \frac{3}{2b^2} \int_0^N ds \left| \frac{d\mathbf{r}_i(s)}{ds} \right|^2 . \tag{4}$$

The non-bonded interaction energies in the model include a set of Flory-Huggins interactions, which may be written in the general form

$$\beta U_1 = \frac{1}{2\rho_0} \int d\mathbf{r} \sum_{i,j} \chi_{ij} \check{\rho}_i(\mathbf{r}) \check{\rho}_j(\mathbf{r}), \tag{5}$$

and the Coulomb interaction is

$$\beta U_c = \frac{l_B}{2} \int d\mathbf{r} \int d\mathbf{r}' \, \frac{\check{\rho}_c(\mathbf{r}) \check{\rho}_c(\mathbf{r}')}{|\mathbf{r} - \mathbf{r}'|}. \tag{6}$$

Here $l_B = \frac{\beta e^2}{4\pi\epsilon_0\epsilon}$ is the Bjerrum length, and $\check{\rho}_c(\mathbf{r})$ is the smeared microscopic charge density, which can in general contain contributions not just from monopole charges, but also from permanent or induced dipoles in order to embed composition-dependent, inhomogeneous dielectric properties.[21,38,40] Finally, the delta functional term in eq 1 enforces an incompressibility constraint.

An important feature of our model is the incorporation of dielectric asymmetry effects. For simplicity, we will assume that all components have the same dielectric constant ϵ, except species A which can have a higher dielectric constant $\epsilon_A = \epsilon + \Delta\epsilon$. We can adjust ϵ_A by assigning a polarizability α_A to monomers of species A, as in recent work.[21,39,41] However, even in such a 'polarizable' field theory, the mean-field approximation (equivalent to Poisson-Boltzmann theory) misses the important effect of the ion solvation energies, which are a component of the ion self-energies and do not arise in the absence of charge fluctuations.[20] Thus, in the mean-field (SCFT) approximation of the model just introduced, the ion solvation effects will not manifest. To address this, we re-insert ion solvation effects into our model using the well-established Born solvation approximation:[15–19]

$$\beta U_b = \frac{l_B^{(0)}}{2} \int d\mathbf{r} \, \frac{1}{\epsilon(\mathbf{r})} \left(\frac{\check{\rho}_+(\mathbf{r})}{a_+} + \frac{\check{\rho}_-(\mathbf{r})}{a_-} \right), \tag{7}$$

where $\epsilon(\mathbf{r}) = \epsilon_A \check{\phi}_A(\mathbf{r}) + \epsilon_B \check{\phi}_B(\mathbf{r}) + \epsilon_+ \check{\phi}_+(\mathbf{r}) + \epsilon_- \check{\phi}_-(\mathbf{r}) = \epsilon + \Delta\epsilon \check{\phi}_A(\mathbf{r})$ is the local dielectric function, $\check{\phi}_j(\mathbf{r}) = \rho_0^{-1} \check{\rho}_j(\mathbf{r})$ is the volume fraction of species j, a_+ and a_- are the radii of the small-molecule ions, and $l_B^{(0)}$ is the *vacuum* Bjerrum length.[45] This expression, however, is not suitable for the Hubbard-Stratonovich transformation that we use to construct our field theories, for which interaction energies must be quadratic in the composition variables. To render eq 7 in an appropriate form, we write $\epsilon(\mathbf{r}) = \epsilon \left(1 + \frac{\Delta\epsilon}{\epsilon} \check{\phi}_A(\mathbf{r})\right)$ and Taylor expand $\epsilon^{-1}(\mathbf{r})$ in powers of $\frac{\Delta\epsilon}{\epsilon} \check{\phi}_A(\mathbf{r})$, keeping only the leading term. The Born solvation energy becomes

$$\begin{aligned} \beta U_b &\approx \frac{l_B}{2} \int d\mathbf{r} \left(\frac{\check{\rho}_+(\mathbf{r})}{a_+} + \frac{\check{\rho}_-(\mathbf{r})}{a_-} \right) \left(1 - \frac{\Delta\epsilon}{\epsilon} \check{\phi}_A(\mathbf{r}) \right) \\ &\approx \frac{l_B n_+}{2a_+} + \frac{l_B n_-}{2a_-} - \frac{l_B \Delta\epsilon}{2\epsilon a_+ \rho_0} \int d\mathbf{r} \, \check{\rho}_+(\mathbf{r}) \check{\rho}_A(\mathbf{r}) - \frac{l_B \Delta\epsilon}{2\epsilon a_- \rho_0} \int d\mathbf{r} \, \check{\rho}_-(\mathbf{r}) \check{\rho}_A(\mathbf{r}). \end{aligned} \tag{8}$$

The first two terms in eq 8 produce constant shifts in the chemical potential of the counterions and may be discarded. The remaining two terms, however, have the form of a Flory-Huggins interaction and are now suitable for the Hubbard-Stratonovich transformation. We can identify associated χ parameters as

$$\chi_{+A} = -\frac{l_B \Delta\epsilon}{2\epsilon a_+}, \qquad \chi_{-A} = -\frac{l_B \Delta\epsilon}{2\epsilon a_-}, \tag{9}$$

the negative values indicating that ion solvation tends to draw counterions into higher-dielectric A-rich domains, as expected. For these ion solvation χ parameters, we will assume for simplicity that the ion radii for both counterions are the same, $a_+ = a_- = a_i$, such that $\chi_{+A} = \chi_{-A}$. For a reasonably bulky counterion such as TFSI ($a_i \approx 0.5$ nm), the ratio l_B/a_i could be as small as ~ 1 (for high-dielectric, e.g. aqueous, systems) or as large as ~ 50 for low-dielectric systems at room temperature. Since we are envisioning a system that is non-aqueous but with bulky counterions and a relatively large dielectric constant, we set $l_B/a_i = 6$ in this work, somewhere in the intermediate range. For example, if the dielectric contrast is $\epsilon_A/\epsilon_B = 2$, this leads to ion solvation parameters $\chi_{+A} = \chi_{-A} = -3$; of course, these parameters could be much larger for more compact ions (such as Li^+). When we account for the solvation χ parameters, the matrix χ_{ij} in eq 5 has only two un-equal nonzero elements, corresponding to interactions either between A and B (χ_{AB}) or between A and the counterions ($\chi_{\pm A}$).

Field-theoretic model and self-consistent field theory (SCFT)

We can now apply the standard field theory transformation,[46] and introduce a set of auxiliary fields that mediate the non-bonded interactions in the model. Following the procedure in Ref. 47, we use the incompressibility constraint to eliminate $\rho_-(\mathbf{r})$ from the interaction energies in eq 5, resulting in a reduced 3×3 contact interaction matrix that has one redundant (zero-eigenvalue) normal mode. After diagonalizing this matrix and performing the Hubbard-Stratonovich transformation, the resulting field-theoretic canonical partition function takes the form

$$\mathcal{Z}_c = \mathcal{Z}_0 \int \mathcal{D}w_+ \int \mathcal{D}w_1 \int \mathcal{D}w_2 \int \mathcal{D}\varphi \, e^{-H[w_+,w_1,w_2,\varphi]}, \tag{10}$$

where w_+ enforces local incompressibility, w_1 and w_2 are the non-redundant exchange-mapped[47] chemical potential fields responsible for the contact (χ_{ij}) interactions, and φ is the electrostatic potential field. The pre-factor $\mathcal{Z}_0$ contains the ideal gas terms from eq 1, and normalization factors from the Hubbard-Stratonovich transforms. The Hamiltonian $H[w_+, w_1, w_2, \varphi]$ is given by

$$\begin{aligned} H[w_+, w_1, w_2, \varphi] = & \frac{\rho_0}{2} \sum_{i=1}^{2} \frac{1}{|\mu_i|} \int d\mathbf{r}\, w_i^2(\mathbf{r}) + \rho_0 \sum_{i=1}^{2} \frac{\xi_i}{\mu_i} \Phi_{iA} \chi_{-A} \int d\mathbf{r}\, w_i(\mathbf{r}) \\ & - i\rho_0 \int d\mathbf{r}\, w_+(\mathbf{r}) + \frac{1}{8\pi l_B} \int d\mathbf{r}\, |\nabla\varphi|^2 \\ & - n_A \ln Q_A[\Omega_A] - n_B \ln Q_B[\Omega_B] - n_+ \ln Q_+[\Omega_+] - n_- \ln Q_-[\Omega_-], \end{aligned} \tag{11}$$

where μ_i and Φ_{ij} are the i^{th} eigenvalue and eigenvector of the reduced contact interaction matrix, and ξ_i takes the value 1 or i for corresponding eigenvalues $\mu_i < 0$ or $\mu_i > 0$, respectively. The $Q[\Omega]$ terms are the single-molecule partition functions. These include single-chain partition functions $Q_{A/B}[\Omega_{A/B}]$:

$$Q_{A/B}[\Omega_{A/B}] = \frac{1}{V} \int d\mathbf{r}\, q_{A/B}(\mathbf{r}, N; [\Omega_{A/B}]), \tag{12}$$

where $q_{A/B}(\mathbf{r}, s; [\Omega_{A/B}])$ is the single-chain propagator that satisfies the following modified diffusion equation

$$\frac{\partial}{\partial s} q_{A/B}(\mathbf{r}, s) = \left[\frac{b^2}{6} \nabla^2 - \Omega_{A/B}(\mathbf{r}) \right] q_{A/B}(\mathbf{r}, s), \tag{13}$$

subject to the initial condition $q_{A/B}(\mathbf{r}, 0) = 1$, and which is solved for s in the range 0–N. The $\Omega_{A/B}(\mathbf{r})$ is a species-dependent auxiliary potential field that contains contributions from the various w and φ fields

$$\Omega_{A/B}(\mathbf{r}) = i\bar{w}_+(\mathbf{r}) + \sum_{i=1}^{2} \xi_i \Phi_{iA/B} \bar{w}_i(\mathbf{r}) + \frac{\alpha_{A/B}}{2l_B} |\nabla\bar{\varphi}|^2 + i\sigma_{A/B}\bar{\varphi}(\mathbf{r}), \tag{14}$$

where the overbar on the fields indicates that they have been smeared via convolution with the Gaussian function $\Gamma(\mathbf{r})$. The α_A is an excess polarizability volume that generates the additional contribution $\Delta\epsilon$ to ϵ_A, and we set $\alpha_B = 0$ since the reference dielectric constant ϵ already accounts for the polarizabilities of the other components. The counterion partition functions are given by

$$Q_\pm[\Omega_\pm] = \frac{1}{V} \int d\mathbf{r} \, \exp\left[-\Omega_\pm(\mathbf{r})\right], \tag{15}$$

where the counterion auxiliary potential fields are

$$\Omega_+(\mathbf{r}) = i\bar{w}_+(\mathbf{r}) + \sum_{i=1}^{2} \xi_i \Phi_{i+} \bar{w}_i(\mathbf{r}) + i\bar{\varphi}(\mathbf{r}), \tag{16}$$

$$\Omega_-(\mathbf{r}) = i\bar{w}_+(\mathbf{r}) - i\bar{\varphi}(\mathbf{r}). \tag{17}$$

In SCFT[46,48,49] we assume that the functional integral comprising the partition function in eq 10 is dominated by a single set of field configurations $\{w_+^*(\mathbf{r}), w_1^*(\mathbf{r}), w_2^*(\mathbf{r}), \varphi^*(\mathbf{r})\}$. These configurations satisfy the so-called *saddle-point equations*

$$\left.\frac{\delta H}{\delta w_i^*(\mathbf{r})}\right|_{\{w^*\},\varphi^*} = 0,$$
$$\left.\frac{\delta H}{\delta w_+^*(\mathbf{r})}\right|_{\{w^*\},\varphi^*} = 0,$$
$$\left.\frac{\delta H}{\delta \varphi^*(\mathbf{r})}\right|_{\{w^*\},\varphi^*} = 0. \tag{18}$$

Within the saddle-point approximation, the partition function simplifies to

$$\mathcal{Z}_c \approx \mathcal{Z}_0 \, e^{-H[w_+^*(\mathbf{r}), w_1^*(\mathbf{r}), w_2^*(\mathbf{r}), \varphi^*(\mathbf{r})]}, \tag{19}$$

and the free energy is given by

$$\beta F = -\ln \mathcal{Z}_0 + H[w_+^*(\mathbf{r}), w_1^*(\mathbf{r}), w_2^*(\mathbf{r}), \varphi^*(\mathbf{r})], \tag{20}$$

where the term involving $\mathcal{Z}_0$ is a reference (ideal-gas) free energy. We solve for the saddle-point configurations (eq 18) within a single unit cell of the relevant microphase using a pseudo-spectral steepest-descent scheme, with a semi-implicit Seidel scheme for field updates and a variable-cell method to locate the zero-stress cell tensor, following a large body of work by some of us.[46,47,50,51] The single-chain propagators are resolved using a contour resolution of $\Delta\tau = \frac{\Delta s}{N} = 0.01$, and the number of grid points along each spatial dimension is in the range $M = 32$–64, which is adjusted according to the convergence requirements of the simulation in question, based on the size of the unit cell (some regions of the phase diagram exhibit dilating unit cells and thus require a larger number of spatial grid points). The spatial grids for 1-, 2- and 3-dimensional phases are M, M^2 and M^3, respectively, with the exception of the σ phase, which uses a $2M \times 2M \times M$ grid. The relaxation of fields and stresses are carried out to within tolerances of 10^{-5} and 10^{-4}, applied to the $L2$-norm of the residuals of the fields and the stress tensor, respectively.

Results

Electrostatically-stabilized microphase separation

Since this system can exhibit either macro- or microphase separation, it is important to begin by establishing the conditions favorable to each. Generally speaking, the system's tendency to macro- or microphase separate is determined by a competition between electrostatics and counterion entropy; that is, whether or not the counterions give up their entropy in order to charge-neutralize the phase-separating domains. If they do not, the resulting domains accumulate charge as they grow and macrophase separation is accompanied by a diverging electrostatic energy cost and is thus prohibited, leading instead to the formation of microphases. In the counterion-free system, microphases are therefore guaranteed unless, trivially, the polymers are themselves charge-neutral (corresponding to the conventional macrophase separating binary homopolymer blend). In the presence of counterions, a large electrostatic strength (i.e. large l_B) will favor charge-neutralization and thus macrophase separation, as will the addition of excess counterions/salt. Conversely, the removal of counterions from the system, relative to the stoichiometric case, will favor microphase separation, as will a large bulk dielectric constant (or small l_B).

Initially, we explore the role of the electrostatic parameters in this system using the random phase approximation (RPA),[52] the details of which are provided in the Appendix. In the RPA, we expand the Hamiltonian in powers of the fields, and truncate at quadratic order. The partition function of the resulting field theory is Gaussian and may be solved analytically. Here we compute the structure factor $S_{AA}^{(RPA)}(k)$, and use it to compute the spinodal (where $S_{AA}^{(RPA)}(k)$ becomes singular), as well as the boundary between micro- and macrophase separating regions (i.e., the boundary between $k^* \neq 0$ and $k^* = 0$ where k^* is the critical wavevector for which $S_{AA}^{(RPA)}(k)$ is a maximum).

Figure 1a demonstrates how the electrostatic strength and the counterion concentration affect the transition from micro- to macrophase separation. For simplicity, we initially consider a symmetric blend, with equal and opposite charge densities ($\sigma_A = -\sigma_B = \sigma$), equal volume fractions ($\phi_A = \phi_B = \phi_p/2$, where ϕ_p is the total polymer volume fraction) and equal dielectric constants ($\epsilon_A = \epsilon_B = \epsilon$). The electrostatic strength can be described using the parameter $\gamma = 4\pi l_B \rho_0 b^2/6$; this is a dimensionless group that naturally emerges in our RPA analysis. Figure 1a plots the value γ_t at the transition as a function of the reduced counterion volume fraction parameter $\phi_i/\sigma\phi_p$ (here ϕ_i is the total volume fraction of small-molecule ions, and we note that $\phi_i/\sigma\phi_p = 1$ corresponds to the salt-free stoichiometric case and is denoted by the grey dashed line). There is a weak (and relatively unimportant) dependence of γ_t on $\chi_{AB}N$, which indicates that whether micro- or macrophase separation is favored is mostly determined by the other (electrostatic) parameters γ and $\phi_i/\sigma\phi_p$. The various colors in Figure 1 correspond to different charge densities, and suggest that it may be easier to access the region of microphase separation (which we are interested in here) by considering systems with lower charge density. Figure 1a suggests that values of $\gamma \lesssim 1$ are probably required to remain in the microphase-separating regime, unless the removal of a significant proportion of counterions can be achieved experimentally. Since the parameter γ depends on dielectric constant, temperature, density and the statistical segment length, it could vary significantly from system to system, but values of $\mathcal{O}(1)$ should be achievable in high-dielectric-constant PILs. We note in particular that a number of measurements[53,54] of PILs have indicated that very high static dielectric constants ($\epsilon \approx 50$–100) are possible.

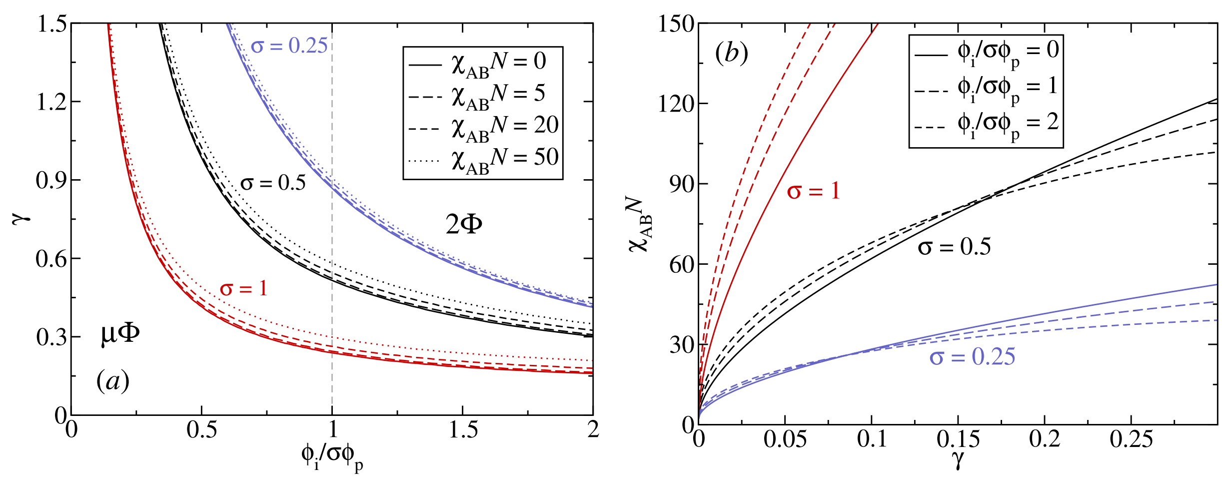

Figure 1: a) Microphase ($\mu\Phi$) to macrophase (2Φ) separation transition γ_t versus counterion volume fraction $\phi_i/\sigma\phi_p$, for high ($\sigma = 1$, red), medium ($\sigma = 0.5$, black) and low ($\sigma = 0.25$, blue) charge densities. b) Critical value of $\chi_{AB}N$ versus the electrostatic strength γ, for the counterion free case ($\phi_i/\sigma\phi_p = 0$), the stoichiometric blend ($\phi_i/\sigma\phi_p = 1$), and a system with excess counterions ($\phi_i/\sigma\phi_p = 2$). a) and b) use $a = 0.2R_g$, and $N = 100$.

In Figure 1b, we plot the critical value $(\chi_{AB}N)_c$, for the onset of phase separation, as a function of electrostatic strength γ, for the counterion free system (solid line), the stoichiometric blend (long dashes), and a system with excess counterions/salt (short dashes). In all cases, $(\chi_{AB}N)_c$ increases significantly with electrostatic strength γ, reflecting the large driving force to phase separate that is required in order to overcome the electrostatic preference for the uniform phase. We also note that for all three cases the macrophase separation regime lies off the range of the axes, meaning that these transitions are to ordered (and due to the symmetry, lamellar) microphases. Also, in all three cases, the addition of counterions increases $(\chi_{AB}N)_c$ when γ is small, but decreases $(\chi_{AB}N)_c$ when γ is large. The former is due to dilution[21,55] (since the counterions occupy volume fraction ϕ_i and their dilution of the polymers is the dominant effect when the electrostatic interactions are weak), while the latter is due to electrostatic screening, wherein the counterions screen the electrostatic interaction between the polyions, making the system phase separate more easily (recall that the electrostatic interaction between polyions favors mixing, i.e. the disordered phase). The results in Figure 1b also indicate that if the charge density on the polymers is high, rather large values of $\chi_{AB}N$ are required in order to phase separate. Synthetically this would require either high-χ backbones or large molecular weights, which might prove undesirable, and so lower charge densities are preferred for the experimental realization of this system.

Phase behavior of the electrostatically symmetric system

Having broadly established the criteria for microphase separation in our model, we now turn to SCFT to examine the phase behavior in greater detail. We restrict ourselves to the microphase separating regime where the most interesting features appear. Throughout, we fix the counterion compositions to their stoichiometric values ($\phi_+/\sigma_B\phi_B = 1$, $\phi_-/\sigma_A\phi_A = 1$), and for simplicity we begin by considering the symmetric ($\sigma_A = -\sigma_B = 0.5$, $\Delta\epsilon = 0$) case. We set a low electrostatic strength of $\gamma = 1.5 \times 10^{-2}$, deep within the microphase region. We note that this small value of γ is probably somewhat lower than achievable experimental values of γ, but it ensures (in general) reasonable domain sizes, so that the SCFT calculations do not become too computationally expensive due to requiring a large number of spatial grid points. We expect our conclusions about the phase behavior at low γ to transfer also to higher values of γ, and that the main effect of increasing γ should be to shift the phase envelope to larger values of $\chi_{AB}N$ (as indicated in Figure 1b) and to globally change the domain sizes of the microphases.

In Figure 2a, we present the phase diagram for this system, which exhibits regions of stability for the lamellar (L), cylindrical (C), gyroid (G), body-centered cubic (BCC) and face-centered cubic (FCC) sphere phases. This largely resembles the phase diagram of the diblock copolymer, which is expected and is essentially in agreement with previous work,[35] although we note that here we have relaxed several approximations that have been made previously (such as the weak segregation assumption, and neglect of counterions as well as neglect of more complicated phases such as gyroid). We also plot the RPA spinodal in Figure 2 (dotted line), which is clearly in agreement with our SCFT results at the critical point and provides additional confidence that our SCFT results are correct. Note that on the composition axis we combine the volume fraction of the polymer species A and its corresponding counterion volume fraction (in this case, the anion), so that the axis sweeps from 0 to 1 as in a traditional diblock copolymer or binary blend phase diagram (we will use this composition axis convention throughout).

Figure 2b shows the free energies, relative to BCC, of FCC, C, and the Frank-Kasper (FK) phases σ and $A15$, for $\chi_{AB}N = 34$ (solid lines) and $\chi_{AB}N = 50$ (dashed lines). Since in traditional block copolymers some source of asymmetry (such as conformational asymmetry) is typically required to stabilize σ and $A15$,[56,57] it is not surprising that these phases do not appear to have regions of stability for the electrostatically-symmetric blend. At first glance, the appearance of a transition from the disordered phase (DIS) to FCC at large $\chi_{AB}N$ (seen in Figure 2a) would seem to merely reaffirm the analogy with the diblock copolymer, which also exhibits that feature. However, in the diblock copolymer the FCC window remains narrow as $\chi_{AB}N$ is increased, but in the charged polymer blend we observe a significant widening of the FCC window, and Figure 2b shows that at high enough $\chi_{AB}N$ (in this case, at $\chi_{AB}N = 50$) the BCC stability window has vanished entirely and a direct $FCC - C$ transition is seen.

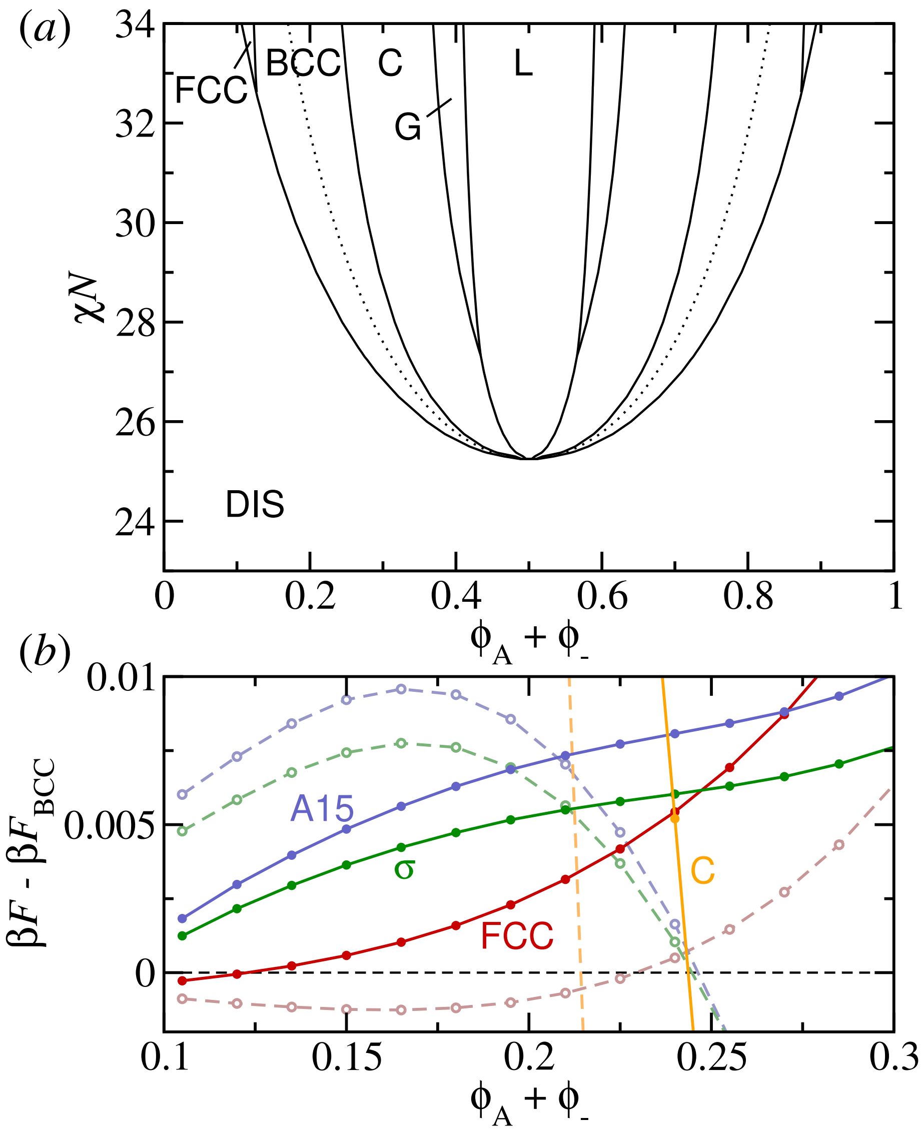

Figure 2: a) SCFT phase diagram of binary blends of electrostatically-symmetric ($\sigma_A = -\sigma_B = 0.5$, $\epsilon_A = \epsilon_B$) polymers. The system contains the stoichiometric counterion compositions, and uses $\gamma = 1.5 \times 10^{-2}$, $a = 0.2R_g$, and $N = 100$. The RPA spinodal is shown as a dotted line. b) Relative free energies $\beta F - \beta F_{BCC}$ of FCC (red), C (orange), $A15$ (blue) and σ (green), at $\chi_{AB}N = 34$ (solid lines/filled symbols) and $\chi_{AB}N = 50$ (dashed lines/hollow symbols).

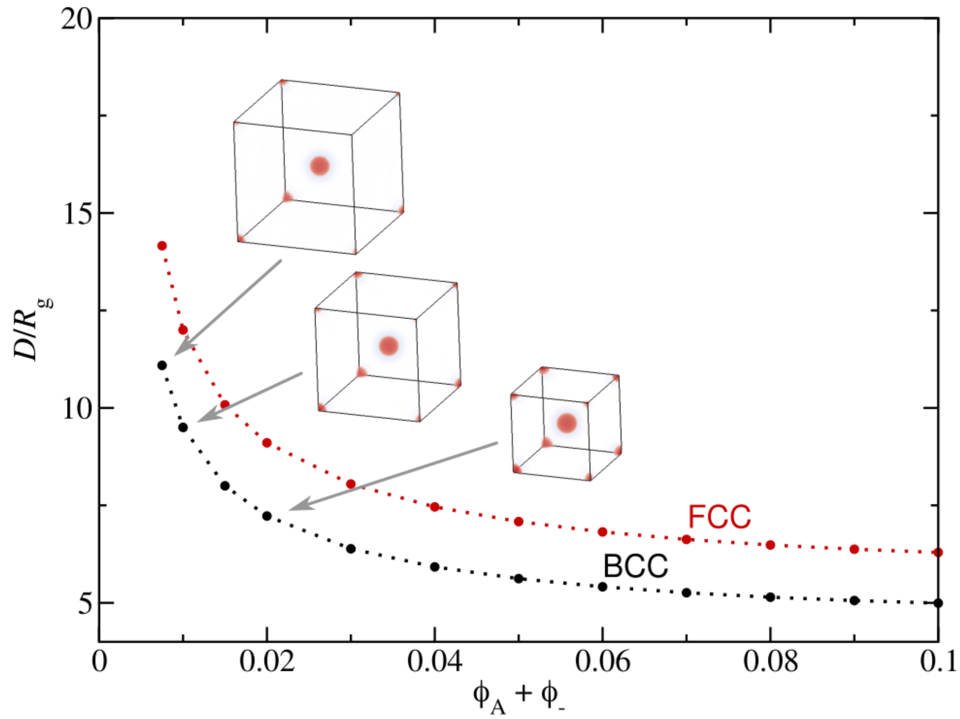

Figure 3: Domain spacing of spherical phases BCC (black) and FCC (red) versus composition $\phi_A + \phi_-$ at $\chi_{AB}N = 50$ in the electrostatically-symmetric blend, showing unit cell dilation at small compositions of A. The inset density plots show examples of $\phi_A(\mathbf{r})$ for converged BCC unit cells at $\phi_A + \phi_- = 0.0075$, 0.01 and 0.02.

Another interesting feature of the spherical phases appears at high $\chi_{AB}N$: at or near the order-disorder transition (ODT), the unit cells dilate dramatically. This is demonstrated in Figure 3, which shows the dependence of domain spacing on the composition for BCC and FCC phases at $\chi_{AB}N = 50$. Below $\phi_A + \phi_- = 0.02$, the domain spacings increase rapidly to well above $D = 10R_g$, meaning that it becomes difficult to accurately resolve the ODT when $\chi_{AB}N$ is large. For this reason, we cut off the SCFT phase diagram in Figure 2a at $\chi_{AB}N = 34$. The insets in Figure 3 show snapshots of the species A density in the converged BCC unit cells, which show that as the unit cell dilates, the spherical domains do not change in size significantly but become further apart as the volume fraction is reduced. Such dilation would be strongly disfavored in a diblock copolymer due to the free energy penalty of stretching the chains to such an extreme. Here there is no such chain-stretching requirement, which appears to allow these dilated unit cells and a phase envelope that may extend to very small values of $\phi_A + \phi_-$ as $\chi_{AB}N$ is increased. These features suggest the possibility of an unbinding transition in this region, although the numerical difficulty in resolving and tracking the structures make it difficult to be conclusive. In any case, these swollen structures are probably susceptible to thermal fluctuations, so a fluctuation-corrected phase diagram, computed via FTS,[58] could reveal that these regions are truncated and replaced with unstructured DIS or a disordered spherical micelle phase.

Effects of electrostatic asymmetry

Next, we consider the effects of electrostatic asymmetries, such as charge asymmetry ($\sigma_A \neq -\sigma_B$) and dielectric asymmetry ($\epsilon_A \neq \epsilon_B$). The reasons to consider this are two-fold: i) practically speaking, any experimental realization of the charged polymer blend will not be precisely symmetric either in terms of charge densities or dielectric constants, so it is useful to understand how *inevitable* electrostatic asymmetries might affect the phase behavior, and ii) to the degree that such asymmetries do affect the phase behavior, it could then be desirable to exploit these effects to manipulate the phase behavior in an experimentally facile way (e.g. by adjusting charge densities or by adding excess salt). In fact, the charge physics that leads to microphase separation in these systems does not even require that the two polymer species have opposite charge densities, since the same effect can be achieved by a polycation-polycation or polyanion-polyanion blend as long as the two polyions have different charge densities (recall that the counterions will maintain overall charge neutrality of the system). Even a blend of a polyion with a charge-neutral polymer should in principle be able to exhibit microphases as long as the counterions are willing to pervade the charge-neutral polymer domains,[31] although this may be difficult to achieve in practice, due to e.g. ion solvation effects, unless the charge-neutral polymer has a rather high dielectric constant.

In light of this, we will now explore the effects of introducing asymmetry in the polymer charge densities. In order to facilitate a meaningful comparison with the charge-symmetric case described above, we will adjust charge densities in such a way that the total number of backbone-tethered ions, and thus the total number of counterions, remains fixed. In other words, we will adjust σ_A and σ_B while satisfying the constraint $|\sigma_A| + |\sigma_B| = 1$; the degree of charge asymmetry can thus be described by $\sigma_A + \sigma_B$, which is zero for a charge-symmetric system and non-zero otherwise as long as $\sigma_A \geq 0$ and $\sigma_B \leq 0$, as is the case here, or vice versa.

We expect that as the charge asymmetry is varied, the phase behavior will differ the most from the charge-symmetric case for the largest deviations of $\sigma_A + \sigma_B$ from zero. Thus in Figure 4a we plot the SCFT phase diagram for the most charge-asymmetric case ($\sigma_A + \sigma_B = 1$), corresponding to $\sigma_A = 1$, $\sigma_B = 0$ so that polymer B is in fact charge neutral. The phase diagram for the charge-symmetric system is also plotted, in grey, to facilitate comparison. In order to isolate the effects of charge asymmetry, we assume that the dielectric constants are the same (noting that it may be unlikely to have charge-neutral and charged polymers with similar dielectric constants, and that we will explore dielectric contrast effects next). Figure 4a shows that, relative to the charge-symmetric case, the critical point shifts to a lower value of $\chi_{AB}N$ (which is confirmed by RPA, also plotted) and larger compositions $\phi_A + \phi_-$.

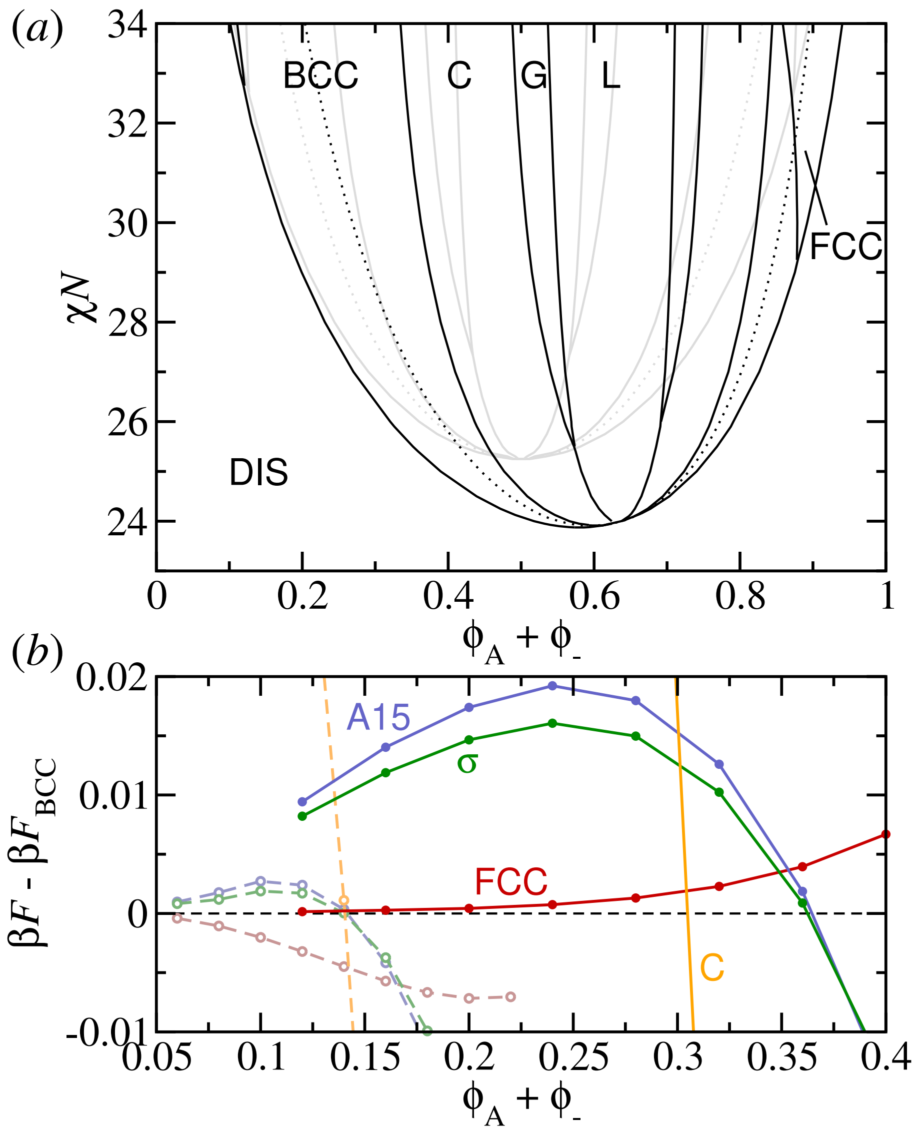

Figure 4: a) SCFT phase diagram of the charge-asymmetric ($\sigma_A = 1$, $\sigma_B = 0$) binary blend. The system contains the stoichiometric counterion compositions, and uses $\gamma = 1.5 \times 10^{-2}$, $a = 0.2R_g$ and $N = 100$. The RPA spinodal is shown as a dotted line, and the charge-symmetric case is included in gray for comparison. b) Relative free energies $\beta F - \beta F_{BCC}$ of FCC (red), C (orange), $A15$ (blue) and σ (green), for charge-asymmetric cases $\sigma_A + \sigma_B = 1$ (solid lines/filled symbols) and $\sigma_A + \sigma_B = -1$ (dashed lines/hollow symbols), at $\chi_{AB}N = 50$.

The latter is mainly due to the fact that the higher charge density of polymer A necessitates a higher volume fraction of associated counterions ϕ_-. Indeed, the phase boundaries in this system shift to the right in composition significantly, relative to the charge-symmetric case, due to this effect.

Overall, other than these shifts in the phase envelope and phase boundaries, the phase diagram in Figure 4 is not too different from the charge-symmetric case. The most striking effect of charge asymmetry is to change which spherical phases are favored near the ODT. Evidently, when the sphere-forming domains are rich in the *charged* polymer, the BCC phase becomes favored over FCC, whereas if the sphere-forming domains are rich in the *charge-neutral* polymer, the FCC phase is favored. In the $\sigma_A + \sigma_B = 1$ case, this produces a strong preference, and a very wide phase window, for FCC on the right side of the phase diagram, suggesting a possible route to stabilizing close-packed spheres experimentally in these systems.

Since the main effect of charge asymmetry on the phase behavior seems to be to change the relative stability of spherical phases, it is reasonable to ask whether these effects can stabilize Frank-Kasper phases. To answer this question, we performed spot-checks on the σ and $A15$ phases at $\chi_{AB}N = 50$, as in Figure 2b. The results are presented in Figure 4b, where we examine both charge-asymmetric extremes $\sigma_A + \sigma_B = 1$ (solid lines, filled symbols) and $\sigma_A + \sigma_B = -1$ (dashed lines, hollow symbols), corresponding effectively to the left and right sides of the phase diagram in Figure 4a. However, our results indicate that charge-asymmetry effects alone are not sufficient to stabilize the FK phases.

These "extreme" cases of charge asymmetry, where one of the polymers is charge neutral, may not be a realistic or practical experimental target for reasons we have identified above. However, the trends identified in Figure 4 transfer to (or rather, are a limiting case of) the more realistic case in which one polyion has a high charge density and the other has a low charge density. In Figure 5a, we explore the charge-asymmetry parameter $\sigma_A + \sigma_B$ more thoroughly, at fixed $\chi_{AB}N = 34$, and show that this is indeed the case. As $\sigma_A + \sigma_B$ is varied from -1 to 1, σ_A is increasing from 0 to 1, and the order-order transition boundaries shift to the right in accordance with the increase in ϕ_- that is required to globally charge-neutralize species A. The size of the phase stability windows do not change substantially, except for the FCC and BCC phases. The overall phase diagram exhibits a point reflection symmetry about the center $(\phi_A + \phi_-, \sigma_A + \sigma_B) = (0.5, 0)$, due to the inherent charge symmetry of the Coulomb interaction. Consistent with our discussion above, FCC becomes stabilized relative to BCC when the sphere-forming domains are rich in the polyion with the lower charge density.

Next we will consider the effects of dielectric contrast. In order to isolate the dielectric effects from the charge density effects, we return initially to the charge-symmetric case $\sigma_A + \sigma_B = 0$. The polarizable field theory framework allows us to increase the component dielectric constant ϵ_A by granting beads of polymer species A some polarizability α_A. As some of us have shown in a previous work,[38] in mean-field theory the incorporation of polarizabilities leads to the same linear constitutive law for the dielectric constant as has been commonly used in the literature for many years. In particular, in the absence of density smearing ($a \to 0$, $\Gamma(\mathbf{r}-\mathbf{r}') \to \delta(\mathbf{r}-\mathbf{r}')$), the local *mean-field* dielectric constant for our system is given by

$$\frac{\epsilon(\mathbf{r})}{\epsilon} = \frac{\epsilon_A}{\epsilon}\phi_A(\mathbf{r}) + \phi_B(\mathbf{r}) + \phi_+(\mathbf{r}) + \phi_-(\mathbf{r}), \tag{21}$$

where $\frac{\epsilon_A}{\epsilon} = 1 + 4\pi\rho_0\alpha_A$, and α_A is the excess polarizability volume of species A, which is the parameter that we manipulate to control the ratio ϵ_A/ϵ_B.

The SCFT phase diagram in Figure 5b shows how dielectric contrast affects phase behavior in the charge-symmetric system at $\chi_{AB}N = 34$, with $l_B/a_i = 6$. Dielectric contrast induces rather dramatic deflections in the phase boundaries, particularly the ODT and the OOTs involving sphere phases. These deflections are primarily caused by the ion solvation effects, which favor the disordered phase when the dielectric contrast is weak (causing the phase envelope to retreat with increasing dielectric contrast) and favor ordered phases when the dielectric contrast is strong (causing the phase envelope to advance with increasing di-

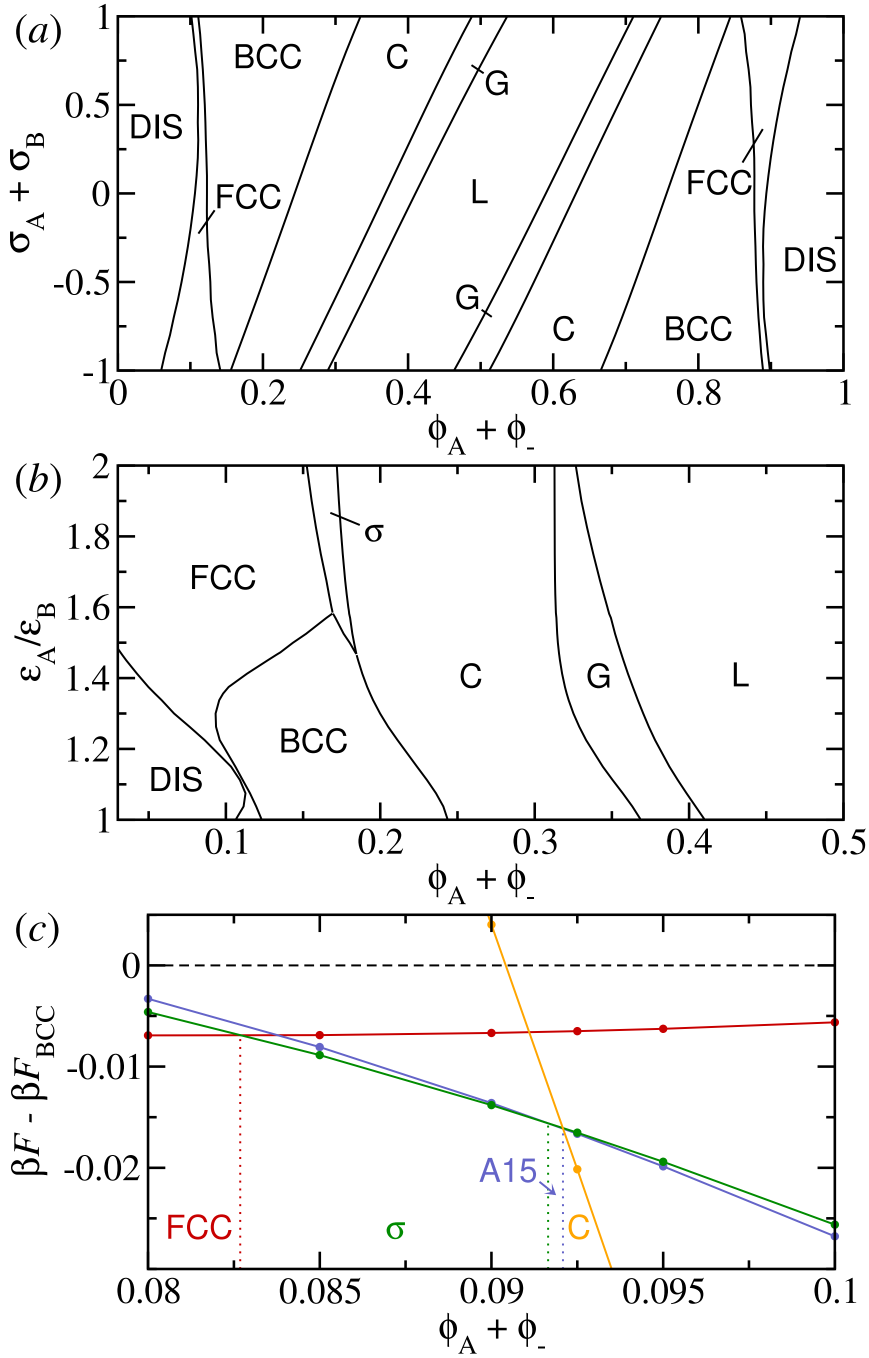

Figure 5: a) SCFT phase diagram of binary blends of charged polymers, at $\chi_{AB}N = 34$, as a function of charge-asymmetry $\sigma_A + \sigma_B$, for the zero dielectric contrast case. b) SCFT phase diagram of binary blends of charged polymers, at $\chi_{AB}N = 34$, as a function of dielectric contrast ϵ_A/ϵ_B, for the charge-symmetric case. c) Relative free energies $\beta F - \beta F_{BCC}$ of FCC (red), C (orange), $A15$ (blue) and σ (green), for a system with combined charge asymmetry ($\sigma_A + \sigma_B = -1$) and dielectric contrast ($\epsilon_A/\epsilon_B = 2$) at $\chi_{AB}N = 34$. OOTs are denoted by dotted vertical lines. a)-c) contain the stoichiometric counterion compositions, and use $\gamma = 1.5 \times 10^{-2}$, $a = 0.2R_g$, and $N = 100$.

electric contrast). These two distinct regimes of ion solvation thermodynamics were first predicted and explained recently by Hou and Qin,[18] who referred to them as "entropic" and "solvation" regimes, respectively. In Figure 5b, the transition from the entropic regime to the solvation regime can be located roughly as the value of ϵ_A/ϵ_B for which the phase envelope goes from retreating to advancing (around $\epsilon_A/\epsilon_B = 1.1$).

The most striking feature of Figure 5b is the appearance of a narrow stability window for the Frank-Kasper σ phase, which appears for values of dielectric contrast $\epsilon_A/\epsilon_B \gtrsim 1.5$. Evidently, if the dielectric constant of the sphere-forming domains is higher than the surrounding matrix, there is a thermodynamic preference for spherical packings with Wigner-Seitz cells (WSCs) that have a high sphericity—features that the Frank-Kasper phases are known to possess. In order to explain why this occurs in this system, let us briefly review the usual mechanism for stabilization of FK phases in block copolymers.[56,59] When the minority domains in a spherical phase are much smaller than the WSC, the WSC has little influence on the shape of those domains. In this case a *BCC* or *FCC* phase can form highly spherical minority domains in order to minimize the interfacial free energy, despite both phases having relatively low-sphericity WSCs. If the minority domains become large enough relative to the WSC, then they will be forced to deform and adopt its shape, and the sphericity of the WSC will then directly determine the excess interfacial area. This will favor the WSCs with higher sphericity: the FK phases. Conditions that stabilize FK phases are thus consistent with those that enlarge discrete minority domains relative to their WSC - this is usually achieved by stabilizing sphere phases, relative to the cylindrical or gyroid phases that typically intervene, at higher volume fractions of the minority component. Block copolymers with conformational asymmetry or architectural frustration (e.g. miktoarm architectures), which favor curvature of the interface toward the minority domains, are the conventional strategy to accomplish this.[51,56,57,59–61]

In contrast to the usual block copolymer strategy to stabilize FK phases, in our system the stabilization of σ, by increasing dielectric contrast, is achieved *without* (in general)

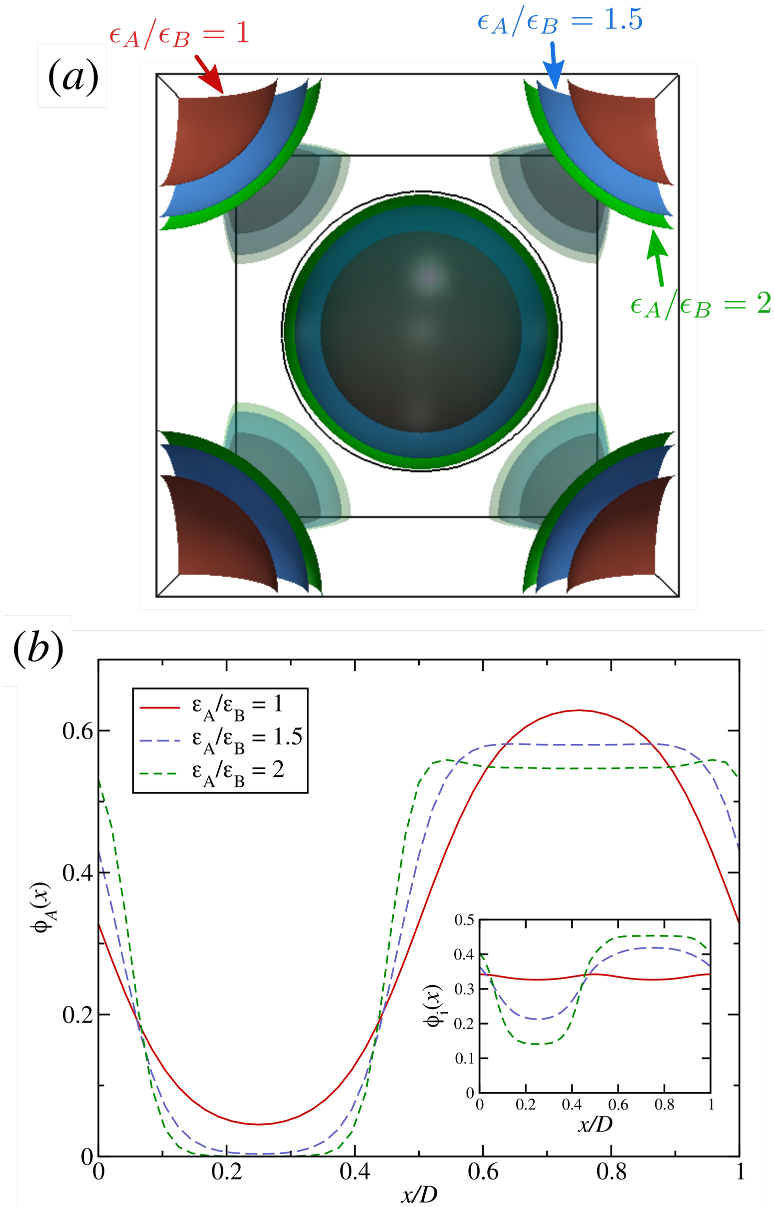

Figure 6: a) Relative size and deformation of spheres in the BCC phase of the charge-symmetric system at $\phi_A + \phi_- = 0.18$, for zero ($\epsilon_A/\epsilon_B = 1$, red), medium ($\epsilon_A/\epsilon_B = 1.5$, blue) and high ($\epsilon_A/\epsilon_B = 2$, green) dielectric contrast. Contour plots correspond to $\phi_A(\mathbf{r}) = \left(\phi_A^{(min)} + \phi_A^{(max)}\right)/2$ for each case. The circle in the center (black) is shown to highlight the asphericity of the larger domains. b) Lamellar phase density profiles $\phi_A(x)$ of the same system at $\phi_A + \phi_- = 0.5$. The corresponding counterion density profiles $\phi_i(x)$ are shown in the inset. Unit cells are normalized in a) and b) in order to control for the change in domain sizes.

pushing the boundary of discrete-minority-domain phases to higher volume fractions. In fact, as Figure 5b shows, the BCC-C (and σ-C) OOTs are shifting to *slightly lower* volume fractions as ϵ_A/ϵ_B is increased. Yet, the stability of σ suggests that the minority component having a higher dielectric constant than the surrounding matrix results in an enlargement of the spherical domains relative to the unit cell. Indeed, in Figure 6a we demonstrate that this is the case, using the BCC phase in the charge-symmetric system (at composition $\phi_A + \phi_- = 0.18$) as an example. The contour plots in Figure 6a correspond to $\phi_A(\mathbf{r}) = \left(\phi_A^{(min)} + \phi_A^{(max)}\right)/2$, and thus delineate the surface of the spherical domains. We note here that the unit cells for the three cases shown ($\epsilon_A/\epsilon_B = 1$, red; $\epsilon_A/\epsilon_B = 1.5$, blue; $\epsilon_A/\epsilon_B = 2$, green) are not the same, so we normalize by the unit cell sizes in order to make a meaningful statement about the sphere sizes *relative* to the WSC, so that the different cases can be compared. Indeed, Figure 6a clearly shows that as the dielectric contrast is increased, not only do the spheres enlarge relative to the WSC, but for the case with the largest dielectric contrast the deformation of the spherical domains can be seen, as they are forced to adopt the shape of the WSC.

The only way it is possible to achieve larger spherical domains without increasing the volume fraction of the minority component is if the composition of the minority (and majority) domains is changing. To illustrate that this is the case, in Figure 6b we plot composition profiles $\phi_A(x)$ (and the counterion density $\phi_i(x) = \rho_0^{-1}\left(\rho_+(x) + \rho_-(x)\right)$ in the inset) in the lamellar phase for the same system and the same values of ϵ_A/ϵ_B as in Figure 6a, but with symmetric composition ($\phi_A + \phi_- = 0.5$), over one lamellar period. For zero dielectric contrast, the lamellar profile is symmetric, as it should be, but as the dielectric contrast is increased the profiles become asymmetric, with the A-rich domains becoming larger (or more 'spread out', with a lower interior volume fraction of A) and the B-rich domains becoming smaller. This is consistent with the idea that higher-dielectric minority domains leads to the enlargement of the spheres relative to the unit cell that is required to stabilize FK phases. The inset of Figure 6b suggests that the counterions are responsible for the change in domain compositions, as the preferential ion solvation drives them to localize into the high-dielectric-constant domains, thus swelling them and leading to the enlargement of spheres in Figure 6a. These results also suggest that on the other side of the phase diagram in Figure 5b (i.e. for $\phi_A + \phi_- > 0.5$) the case $\epsilon_A > \epsilon_B$ is not likely to result in stabilization of FK phases, as the minority domains would then have the *lower* dielectric constant, and Figure 6b indicates that this would result in the *shrinking*, rather than enlargement, of the minority domains relative to the WSC.

Finally, we briefly consider the effects of combining charge asymmetry and dielectric contrast. In Figure 5c, we show the free energies of the sphere phases, as well as C, relative to BCC, for a charge-asymmetric ($\sigma_A + \sigma_B = -1$) system that also has dielectric contrast ($\epsilon_A/\epsilon_B = 2$) at $\chi_{AB}N = 34$, the same value of $\chi_{AB}N$ as Figure 5b. In addition to the relative free energies, Figure 5c shows the order-order transitions as vertical dotted lines. Here we see that in addition to a region of stability for σ, we also obtain a narrow region of stability for $A15$, which is not present at the same $\chi_{AB}N$ in the charge-symmetric case of Figure 5b and indicates that by combining these electrostatic asymmetries one can further manipulate the phase behavior and stabilize, or help to stabilize, additional complex sphere phases.

Conclusions

In this work, we have comprehensively explored the phase behavior of a microphase-separating immiscible charged polymer blend. Using the random phase approximation, we computed the transition from micro- to macrophase separation for a symmetric blend with equal dielectric constants and equal, but opposite, charge densities and showed how the system microphase separates (rather than macrophase separates) when entropy drives the counterions to homogenize through the system, thus preventing them from locally charge-neutralizing the phase-separating domains. The macrophase separation transition is thus determined primarily by a competition between counterion entropy and the electrostatic strength (Bjerrum length). Our RPA results suggest that the proximity to the transition can be increased or decreased by removing counterions (or lowering charge density), or adding salt (or increasing charge density), respectively. Using self-consistent field theory, we then mapped the phase behavior in the microphase separating regime. We found that the electrostatically symmetric system exhibits the same ordered phases and a very similar phase diagram as the canonical diblock copolymer. This is in agreement with previous work by other researchers,[35] who have explored how this arises from the analogous property that the electrostatic interactions in the charged polymer blend and the block connectivity in a block copolymer both prohibit separation of the A and B species on macroscopic scales. However, our SCFT results also highlight key differences from the diblock copolymer, in particular the fact that the FCC phase becomes entirely favored over BCC at large $\chi_{AB}N$ in the charge-symmetric blend.

Next, we considered the effects of asymmetries in the polymer charge densities and dielectric constants. The effects of charge asymmetry are mainly to change the relative stability of FCC and BCC phases near the ODT, causing FCC to be favored even more than in the charge-symmetric case, when the minority (sphere-forming) domains are rich in the polymer with the *lower* charge density. The effects of dielectric contrast are more dramatic, and we showed that they can stabilize the Frank-Kasper σ phase. Enlargement of the spherical domains relative to the unit cell is critical to the stability of FK phases, and in this case the preferential solvation of counterions in the higher-dielectric-constant domains leads to a counterion localization-induced enlargement of spheres when the minority (sphere-forming) component has a higher dielectric constant than the majority component. Distinct from how FK phases are stabilized in more traditional block copolymers, in this system the sphere enlargement is accomplished without the need to increase the overall volume fraction of the minority component, and is accompanied by a change in the composition in the interior of the spheres. Finally, we showed that by combining charge asymmetry with dielectric contrast, the $A15$ phase could be stabilized, in addition to σ. It would be interesting to leverage what has been learned here to investigate whether or not stability windows for other FK phases (e.g. $C14$, $C15$) might be found as well in this system.

The electrostatically-stabilized microphase separation of charged but immiscible polymer blends opens up new routes to achieving ordered phases in polymeric systems. These new routes leverage the fact that the length scale and symmetry of the resulting microstructures are primarily set by the electrostatic interactions rather than the molecular weight or block fraction as in a block copolymer. One advantage of this approach to stabilizing ordered phases is that the composition axis can be explored simply by mixing the two components in different proportions, which does not require synthesizing new materials with a different block fraction or architecture. In addition, the microstructure length-scale can in principle be easily enlarged by adding excess salt to the system. Such electrostatic manipulation of phase behavior could open a route to giant-unit-cell Frank-Kasper phases, bicontinuous microemulsions, or other phases with desirable properties such as photonic bandgaps, chirality, high ionic conductivity, etc., the possibilities for which have presently not been explored but which we hope to address in future work. However, there are probably synthetic challenges associated with finding the right backbone chemistries so that the requirements of immiscibility, relatively high dielectric constants and bulky ionic moieties can be satisfied and realized experimentally. Polymeric ionic liquids (PILs) seem like a natural candidate for realizations of this idea, since their bulky ionic groups should allow them to be thermally tractable and capable of equilibrating as non-aqueous (solvent-free) blends.

Appendix. Random Phase Approximation

We derive the RPA expression for the structure factor $\frac{S_{AA}^{(RPA)}(k)}{N} = \frac{1}{N}\langle\hat{\rho}_A(\mathbf{k})\hat{\rho}_A(-\mathbf{k})\rangle_{RPA}$ using a compressible variant of our model, in which the incompressibility constraint is removed and replaced by a Helfand compressibility interaction energy of the form

$$\beta U_H = \frac{\zeta}{2\rho_0}\int d\mathbf{r}\ (\breve{\rho}(\mathbf{r}) - \rho_0)^2 \tag{22}$$

that penalizes fluctuations of the density away from the bulk average density ρ_0. Note that this compressible model will reduce to an incompressible model that is equivalent to the one we consider above, in the limit $\zeta \to \infty$. When evaluating our final RPA expressions for the spinodal lines and micro- to macrophase separation transition lines in the Results section, we set $\zeta = 10^5$. Since the RPA results are only applied to the electrostatically-symmetric system, we consider only the zero dielectric contrast case here.

We carry out RPA by constructing a density-explicit (rather than auxiliary)[46] field-theory representation of the model, which takes the general form

$$\mathcal{Z}_c = \mathcal{Z}_0 \int \mathcal{D}\rho_A \mathcal{D}\rho_B \mathcal{D}\rho_+ \mathcal{D}\rho_- \mathcal{D}w_A \mathcal{D}w_B \mathcal{D}w_+ \mathcal{D}w_- \, e^{-H[\{\rho_i\},\{w_i\}]}, \tag{23}$$

noting that an explicit electrostatic field is not required in this representation because the charge density may be written entirely in terms of the bead densities of the four components (i.e. $\rho_c(\mathbf{r}) = \sigma_A \rho_A(\mathbf{r}) + \sigma_B \rho_B(\mathbf{r}) + z_+ \rho_+(\mathbf{r}) - z_- \rho_-(\mathbf{r})$). This form of the field theory introduces a density and chemical potential field for each component, resulting in a total of 8 fields. The RPA procedure consists of expanding the Hamiltonian in powers of the fields, assuming weak fluctuations about the homogeneous saddle-point, and truncating at second-order. $S_{AA}^{(RPA)}(k)$ is then computed by integrating out the 7 fields other than ρ_A, leveraging Gaussian integral identities. The calculation is straightforward, albeit tedious, and the result can be written in the general form

$$\begin{aligned}\frac{N}{S_{AA}^{(RPA)}} = {} & \Omega_{AA} - \frac{\Omega_{A-}^2}{\Omega_{--}} - \frac{\left(\Omega_{A+} - \frac{\Omega_{A-}\Omega_{+-}}{\Omega_{--}}\right)^2}{\Omega_{++} - \frac{\Omega_{+-}^2}{\Omega_{--}}} \\ & - \frac{\left[\Omega_{AB} - \frac{\Omega_{A-}\Omega_{B-}}{\Omega_{--}} - \frac{\left(\Omega_{A+} - \frac{\Omega_{A-}\Omega_{+-}}{\Omega_{--}}\right)\left(\Omega_{B+} - \frac{\Omega_{+-}^2}{\Omega_{--}}\right)}{\Omega_{++} - \frac{\Omega_{+-}^2}{\Omega_{--}}}\right]^2}{\Omega_{BB} - \frac{\Omega_{B-}^2}{\Omega_{--}} - \frac{\left(\Omega_{B+} - \frac{\Omega_{B-}\Omega_{+-}}{\Omega_{--}}\right)^2}{\Omega_{++} - \frac{\Omega_{+-}^2}{\Omega_{--}}}},\end{aligned} \tag{24}$$

where $S_{AA}^{(RPA)}$ and all of the functions Ω_{ij} have an implied wavevector-dependence that has been omitted for brevity. The functions Ω_{ij} are given by

$$\Omega_{AA}(k) = \zeta N + \frac{6\gamma N \sigma_A^2}{k^2} + \frac{1}{\phi_A \hat{g}_D(k)\hat{\Gamma}^2(k)} \tag{25}$$

$$\Omega_{AB}(k) = \zeta N + \chi_{AB} N + \frac{6\gamma N \sigma_A \sigma_B}{k^2} \tag{26}$$

$$\Omega_{A+}(k) = \zeta N + \frac{6\gamma N \sigma_A z_+}{k^2} \tag{27}$$

$$\Omega_{A-}(k) = \zeta N - \frac{6\gamma N \sigma_A z_-}{k^2} \tag{28}$$

$$\Omega_{BB}(k) = \zeta N + \frac{6\gamma N \sigma_B^2}{k^2} + \frac{1}{\phi_B \hat{g}_D(k)\hat{\Gamma}^2(k)} \tag{29}$$

$$\Omega_{B+}(k) = \zeta N + \frac{6\gamma N \sigma_B z_+}{k^2} \tag{30}$$

$$\Omega_{B-}(k) = \zeta N - \frac{6\gamma N \sigma_B z_-}{k^2} \tag{31}$$

$$\Omega_{++}(k) = \zeta N + \frac{6\gamma N z_+^2}{k^2} + \frac{1}{\phi_+ \hat{\Gamma}^2(k)} \tag{32}$$

$$\Omega_{+-}(k) = \zeta N - \frac{6\gamma N z_+ z_-}{k^2} \tag{33}$$

$$\Omega_{--}(k) = \zeta N + \frac{6\gamma N z_-^2}{k^2} + \frac{1}{\phi_- \hat{\Gamma}^2(k)}. \tag{34}$$

Here, the wavevector k is in units of b^{-1}, the $\hat{g}_D(k) = \frac{72}{k^4 N^2}\left(e^{-k^2 N/6} - 1 + k^2 N/6\right)$ is the homopolymer Debye function for the polymers A and B, and the function $\hat{\Gamma}(k) = e^{-k^2 a^2/2}$ is the Fourier-transform of the Gaussian density-smearing function.

Acknowledgement

The authors thank Joshua Lequieu for helpful discussions. The research reported here was primarily supported by the National Science Foundation (NSF) through the Materials Research Science and Engineering Center at UC Santa Barbara, DMR-1720256 (IRG-2). The SCFT methods utilized were developed under support from the NSF Condensed Matter and Materials Theory Program under DMR-1822215. Extensive use was also made of the Center for Scientific Computing from the CNSI, MRL: an NSF MRSEC (DMR-1720256) and NSF CNS-1725797.

References

(1) Holden, G.; Legge, N.; Quirk, R.; Schroeder, H. *Thermoplastic Elastomers*, 2nd ed.; Hanser Gardner Publications: Cincinatti, Ohio, U.S.A., 1996.

(2) Stewart, R. J.; Wang, C. S.; Shao, H. Complex coacervates as a foundation for synthetic underwater adhesives. *Adv. Colloid Interface Sci.* **2011**, *167*, 85–93.

(3) Blocher, W. C.; Perry, S. L. Complex coacervate-based materials for biomedicine. *Wiley Interdiscip. Rev.: Nanomed. Nanobiotechnol.* **2017**, *9*, e1442.

(4) Ruzette, A.-V. G.; Soo, P. P.; Sadoway, D. R.; Mayes, A. M. Melt-formable block copolymer electrolytes for lithium rechargeable batteries. *J. Electrochem. Soc.* **2001**, *148*, A537–A543.

(5) Wang, J.-Y.; Chen, W.; Russell, T. P. Ion-complexation-induced changes in the interaction parameter and the chain conformation of PS-*b*-PMMA copolymers. *Macromolecules* **2008**, *41*, 4904–4907.

(6) Young, W.-S.; Kuan, W.-F.; Epps, T. H. Block copolymer electrolytes for rechargeable lithium batteries. *J. Polym. Sci., Part B: Polym. Phys.* **2014**, *52*, 1–16.

(7) Teran, A. A.; Balsara, N. P. Thermodynamics of Block Copolymers with and without Salt. *J. Phys. Chem. B* **2014**, *118*, 4–17.

(8) Grady, B. P. Review and Critical Analysis of the Morphology of Random Ionomers Across Many Length Scales. *Polym. Eng. Sci.* **2008**, *48*, 1029–1051.

(9) Zhang, L.; Brostowitz, N. R.; Cavicchi, K. A.; Weiss, R. A. Perspective: Ionomer Research and Applications. *Macromol. React. Eng.* **2014**, *8*, 81–99.

(10) Yuan, J.; Antonietti, M. Poly(ionic liquids)s: Polymers expanding classical property profiles. *Polymer* **2011**, *52*, 1469–1482.

(11) Green, O.; Grebjesic, S.; Lee, S.; Firestone, M. A. The Design of Polymeric Ionic Liquids for the Preparation of Functional Materials. *Polym. Rev.* **2009**, *49*, 339–360.

(12) Evans, C. M.; Bridges, C. R.; Sanoja, G. E.; Bartels, J.; Segalman, R. A. Role of Tethered Ion Placement on Polymerized Ionic Liquid Structure and Conductivity: Pendant versus Backbone Charge Placement. *ACS Macro Lett.* **2016**, *5*, 925–930.

(13) Nie, H.; Schauser, N. S.; Dolinski, N. D.; Hu, J.; Hawker, C. J.; Segalman, R. A.; de Alaniz, J. R. Light-Controllable Ionic Conductivity in a Polymeric Ionic Liquid. *Angew. Chem. Int. Ed.* **2020**, *59*, 5123–5128.

(14) Xie, S.; Lindsay, A. P.; Bates, F. S.; Lodge, T. P. Formation of a C15 Laves Phase with a Giant Unit Cell in Salt-Doped A/B/AB Ternary Polymer Blends. *ACS Nano* **2020**, *14*, 13754–13764.

(15) Wang, Z.-G. Effects of Ion Solvation on the Miscibility of Binary Polymer Blends. *J. Phys. Chem. B* **2008**, *112*, 16205–16213.

(16) Nakamura, I.; Balsara, N. P.; Wang, Z.-G. First-Order Disordered-to-Lamellar Phase Transition in Lithium Salt-Doped Block Copolymers. *ACS Macro Lett.* **2013**, *2*, 478–481.

(17) Nakamura, I.; Balsara, N. P.; Wang, Z.-G. Thermodynamics of Ion-Containing Polymer Blends and Block Copolymers. *Phys. Rev. Lett.* **2011**, *107*, 198301.

(18) Hou, K. J.; Qin, J. Solvation and Entropic Regimes in Ion-Containing Block Copolymers. *Macromolecules* **2018**, *51*, 7463–7475.

(19) Hou, K. J.; Loo, W. S.; Balsara, N. P.; Qin, J. Comparing Experimental Phase Behavior

of Ion-Doped Block Copolymers with Theoretical Predictions Based on Selective Ion Solvation. *Macromolecules* **2020**, *53*, 3956–3966.

(20) Wang, Z.-G. Fluctuation in electrolyte solutions: The self energy. *Phys. Rev. E* **2010**, *81*, 021501.

(21) Grzetic, D. J.; Delaney, K. T.; Fredrickson, G. H. Field-Theoretic Study of Salt-induced Order and Disorder in a Polarizable Diblock Copolymer. *ACS Macro Lett.* **2019**, *8*, 962–967.

(22) Delaney, K. T.; Fredrickson, G. H. Theory of polyelectrolyte complexation - Complex coacervates are self-coacervates. *J. Chem. Phys.* **2017**, *146*.

(23) Danielsen, S. P. O.; McCarty, J.; Shea, J.-E.; Delaney, K. T.; Fredrickson, G. H. Molecular design of self-coacervation phenomena in block polyampholytes. *Proc. Natl. Acad. Sci. U. S. A.* **2019**, *116*, 8224–8232.

(24) Li, L.; Srivastava, S.; Andreev, M.; Marciel, A. B.; de Pablo, J. J.; Tirrell, M. V. Phase Behavior and Salt Partitioning in Polyelectrolyte Complex Coacervates. *Macromolecules* **2018**, *51*, 2988–2995.

(25) Rathee, V. S.; Sidky, H.; Sikora, B. J.; Whitmer, J. K. Role of Associative Charging in the Entropy-Energy Balance of Polyelectrolyte Complexes. *J. Am. Chem. Soc.* **2018**, *140*, 15319–15328.

(26) Sing, C. E.; Zwanikken, J. W.; de la Cruz, M. O. Electrostatic control of block copolymer morphology. *Nature Mat.* **2014**, *13*, 694–698.

(27) Sing, C. E.; Zwanikken, J. W.; de la Cruz, M. O. Theory of melt polyelectrolyte blends and block copolymers: Phase behavior, surface tension, and microphase periodicity. *J. Chem. Phys.* **2015**, *142*.

(28) Audus, D. J.; Gopez, J. D.; Krogstad, D. V.; Lynd, N. A.; Kramer, E. J.; Hawker, C. J.; Fredrickson, G. H. Phase behavior of electrostatically complexed polyelectrolyte gels using an embedded fluctuation model. *Soft Matter* **2015**, *11*, 1214–1225.

(29) Sing, C. E. Micro- to macro-phase separation transition in sequence-defined coacervates. *J. Chem. Phys.* **2020**, *152*.

(30) Borue, V. Y.; Erukhimovich, I. Y. A statistical theory of weakly charged polyelectrolytes: fluctuations, equation of state and microphase separation. *Macromolecules* **1988**, *21*, 3240–3249.

(31) Dobrynin, A. V.; Erukhimovich, I. Y. Weak crystallization and structural phase transitions in weakly charged polyelectrolyte systems. *J. Exp. Theor. Phys.* **1991**, *72*, 751–759.

(32) Rumyantsev, A. M.; Kramarenko, E. Y. Two regions of microphase separation in ion-containing polymer solutions. *Soft Matter* **2017**, *13*, 6831–6844.

(33) Rumyantsev, A. M.; Kramarenko, E. Y.; Borisov, O. V. Microphase Separation in Complex Coacervate Due to Incompatibility Between Polyanion and Polycation. *Macromolecules* **2018**, *51*, 6587–6601.

(34) Rumyantsev, A. M.; Gavrilov, A. A.; Kramarenko, E. Y. Electrostatically Stabilized Microphase Separation in Blends of Oppositely Charged Polyelectrolytes. *Macromolecules* **2018**, *51*, 6587–6601.

(35) Rumyantsev, A. M.; de Pablo, J. J. Microphase Separation in Polyelectrolyte Blends: Weak Segregation Theory and Relation to Nuclear "Pasta". *Macromolecules* **2020**, *53*, 1281–1292.

(36) Brazovskii, S. A. Phase transition of an isotropic system to a nonuniform state. *Sov. Phys.-JETP* **1975**, *41*.

(37) Fredrickson, G. H.; Helfand, E. Fluctuation effects in the theory of microphase separation in block copolymers. *J. Chem. Phys.* **1987**, *87*.

(38) Martin, J. M.; Li, W.; Delaney, K. T.; Fredrickson, G. H. Statistical field theory description of inhomogeneous polarizable soft matter. *J. Chem. Phys.* **2016**, *145*, 154104.

(39) Grzetic, D. J.; Delaney, K. T.; Fredrickson, G. H. The effective χ parameter in polarizable polymeric systems: One-loop perturbation theory and field-theoretic simulations. *J. Chem. Phys.* **2018**, *148*, 204903.

(40) Grzetic, D. J.; Delaney, K. T.; Fredrickson, G. H. Contrasting Dielectric Properties of Electrolyte Solutions with Polar and Polarizable Solvents. *Phys. Rev. Lett.* **2019**, *122*, 128007.

(41) Schauser, N. S.; Grzetic, D. J.; Tabassum, T.; Kliegle, G. A.; Le, M. L.; Susca, E. M.; Antoine, S.; Keller, T. J.; Delaney, K. T.; Han, S.; Seshadri, R.; Fredrickson, G. H.; Segalman, R. A. The Role of Backbone Polarity on Aggregation and Conduction of Ions in Polymer Electrolytes. *J. Am. Chem. Soc.* **2020**, *142*, 7055–7065.

(42) Martin, J. M.; Delaney, K. T.; Fredrickson, G. H. Effect of an electric field on the stability of binary dielectric fluid mixtures. *J. Chem. Phys.* **2020**, *152*, 234901.

(43) Villet, M. C.; Fredrickson, G. H. Efficient field-theoretic simulation of polymer solutions. *J. Chem. Phys.* **2014**, *141*, 224115.

(44) Technically an incompressible model, even with smeared densities, is still UV divergent. In any future studies using field-theoretic simulations, the incompressibility constraint would also be relaxed.

(45) We have made use of the fact that the system is incompressible; that is, $\check{\phi}_A(\mathbf{r})+\check{\phi}_B(\mathbf{r})+\check{\phi}_+(\mathbf{r})+\check{\phi}_-(\mathbf{r})=1$.

(46) Fredrickson, G. H. *The Equilibrium Theory of Inhomogeneous Polymers*; Oxford University Press: Oxford, 2006.

(47) Düchs, D.; Delaney, K. T.; Fredrickson, G. H. A multi-species exchange model for fully fluctuating polymer field theory simulations. *J. Chem. Phys.* **2014**, *141*, 174103.

(48) Helfand, E. Theory of Inhomogeneous Polymers: Fundamentals of the Gaussian Random-Walk Model. *J. Chem. Phys.* **1975**, *62*, 999–1005.

(49) Matsen, M. W.; Schick, M. Stable and Unstable Phases of a Diblock Copolymer Melt. *Phys. Rev. Lett.* **1994**, *72*.

(50) Barrat, J.-L.; Fredrickson, G. H.; Sides, S. W. Introducing Variable Cell Shape Methods in Field Theory Simulations of Polymers. *J. Phys. Chem. B* **2005**, *109*, 6694–6700.

(51) Lequieu, J.; Koeper, T.; Delaney, K. T.; Fredrickson, G. H. Extreme Deflection of Phase Boundaries and Chain Bridging in $A(BA')_n$ Miktoarm Star Polymers. *Macromolecules* **2020**, *53*, 513–522.

(52) Leibler, L. Theory of Microphase Separation in Block Copolymers. *Macromolecules* **1980**, *13*, 1602–1617.

(53) Choi, U. H.; Mittal, A.; Price, T. L.; Gibson, H. W.; Runt, J.; Colby, R. H. Polymerized Ionic Liquids with Enhanced Static Dielectric Constants. *Macromolecules* **2013**, *46*, 1175–1186.

(54) Choi, U. H.; Price, T. L.; Schoonover, D. V.; Xie, R.; Gibson, H. W.; Colby, R. H. Role of Chain Polarity on Ion and Polymer Dynamics: Molecular Volume-Based Analysis of the Dielectric Constant for Polymerized Norbornene-Based Ionic Liquids. *Macromolecules* **2020**, *53*, 10561–10573.

(55) Qin, J.; de Pablo, J. J. Ordering Transition in Salt-Doped Diblock Copolymers. *Macromolecules* **2016**, *49*, 3630–3638.

(56) Li, W.; Duan, C.; Shi, A.-C. Nonclassical Spherical Packing Phases Self-Assembled from AB-Type Block Copolymers. *ACS Macro Lett.* **2017**, *6*, 1257–1262.

(57) Bates, M. W.; Lequieu, J.; Barbon, S. M.; III, R. M. L.; Delaney, K. T.; Anastasaki, A.; Hawker, C. J.; Fredrickson, G. H.; Bates, C. M. Stability of the A15 phase in diblock copolymer melts. *Proc. Natl. Acad. Sci. U. S. A.* **2019**, *116*, 13194–13199.

(58) Delaney, K. T.; Fredrickson, G. H. Recent Developments in Fully Fluctuating Field-Theoretic Simulations of Polymer Melts and Solutions. *J. Phys. Chem. B* **2016**, *120*, 7615–7634.

(59) Grason, G. M.; DiDonna, B. A.; Kamien, R. D. Geometric Theory of Diblock Copolymer Phases. *Phys. Rev. Lett.* **2003**, *91*, 058304.

(60) Lee, S.; Bluemle, M. J.; Bates, F. S. Discovery of a Frank-Kasper σ phase in sphere-forming block copolymer melts. *Science* **2010**, *330*, 349–353.

(61) Bates, M. W.; Barbon, S. M.; Levi, A. E.; III, R. M. L.; Beech, H. K.; Vonk, K. M.; Zhang, C.; Fredrickson, G. H.; Hawker, C. J.; Bates, C. M. Synthesis and Self-Assembly of AB_n Miktoarm Star Polymers. *ACS Macro Lett.* **2019**, *9*, 396–403.

Graphical TOC Entry